Estimation of the Temporal Evolution of the Deformation Using Airborne Differential SAR Interferometry

Pau Prats, *Member, IEEE*, Andreas Reigber, *Member, IEEE*, Jordi J. Mallorquí, *Member, IEEE*, Rolf Scheiber, and Alberto Moreira, *Fellow, IEEE*

***Abstract*—This paper presents airborne differential synthetic aperture radar (SAR) interferometry results using a stack of 14 images, which were acquired by the Experimental SAR system of the German Aerospace Center (DLR) during a time span of 2.5 h. An advanced differential technique is used to retrieve the error in the digital elevation model and the temporal evolution of the deformation for every coherent pixel in the image. The two main limitations in airborne SAR processing are analyzed, namely, the existence of residual motion errors (RMEs) (inaccuracies in the navigation system on the order of 1–5 cm) and the accommodation of the topography and the aperture dependence on motion errors during the processing. The coupling between them is also addressed, showing that the estimation of the differential RME, i.e., baseline error, can be biased when using techniques based on the coregistration between interferometric looks. The SAR focusing chain to process the data is also presented together with the modifications in the differential interferometry processor to deal with the remaining baseline error. The detected motion of a corner reflector and the measured deformation in several agricultural fields allows one to validate the proposed techniques.**

***Index Terms*—Differential interferometry, interferometry, motion compensation (MoCo), SAR processing, synthetic aperture radar (SAR).**

I. Introduction

DIFFERENTIAL synthetic aperture radar interferometry (DInSAR) has become a powerful tool to measure deformation phenomena at a large scale [1]–[10]. Very high accuracy, on the order of a fraction of the wavelength, can be attained by exploiting the coherent nature of SAR systems. The first differential results were published by Gabriel *et al.* in 1989 [11], where changes in some agricultural fields on the order of some centimeters over approximately one month were detected with Seasat L-band data. By comparing the areas experiencing the detected surface elevation changes with irrigation records, they concluded that these areas were irrigated in between the observations, causing a change in the penetration depth of the electromagnetic waves due to an increase of soil moisture. Later on, Massonnet *et al.* [12] detected and validated in 1993 an earthquake signature using ERS-1 data. Since these breakthrough results, differential interferometry techniques have evolved to become more reliable and accurate.

Indeed, DInSAR using a spaceborne platform is already an established technique. The ideal stable trajectory of a satellite ensures that the SAR processor will be able to properly focus the data without introducing undesired artifacts. In addition, the fact that a large stack of images is available has been of great help to develop several advanced DInSAR (ADInSAR) techniques [1]–[6]. However, the airborne data processing represents a further challenge, since it is subject to the limitations imposed by motion compensation (MoCo). The fact that the platform is not following an ideally rectilinear trajectory causes several errors that must be compensated for achieving the accuracy required for DInSAR.

However, the advantages an airborne platform can offer are quite appealing: flexibility in the sense of spatial resolution, used wavelength, and data acquisition (short revisit time). For example, the radar frequency plays an important role regarding temporal coherence and ground penetration, since lower frequency bands (L, P) tend to have a better long-term coherence and higher ground penetration than higher frequency bands. This required flexibility is provided by several airborne systems, given that they can operate at different frequency bands [13]–[16]. In addition, the flexibility of the data acquisition is a major asset, since the aircraft can be used to acquire the images with the desired time intervals and geometries, without having to wait, as it happens in the orbital case, for the satellite to illuminate the same area with a similar look angle.

There are mainly two limitations in airborne repeat-pass interferometry. The first limitation, addressed in Section II-A, is the fact that a constant reference height for the whole image must be assumed during MoCo if fast Fourier-based processors are to be used. However, several efficient algorithms have been recently developed that precisely take into account topography [17]–[19]. The second, and most important, limitation is the presence of residual motion errors (RMEs), i.e., inaccuracies

Manuscript received June 20, 2007; revised August 23, 2007. This work was supported in part by the Spanish Ministerio de Ciencia y Tecnologia and Fondo Europeo de Desarrollo Regional Funds under Project TEC2005-06863-C02-01.

P. Prats was with the Remote Sensing Laboratory, Universitat Politècnica de Catalunya, 08034 Barcelona, Spain. He is now with the Microwaves and Radar Institute, German Aerospace Center (DLR), 82234 Oberpfaffenhofen, Germany (e-mail: Pau.Prats@dlr.de).

A. Reigber is with the Computer Vision and Remote Sensing Laboratories, Berlin University of Technology, 10587 Berlin, Germany (e-mail: anderl@cs.tu-berlin.de).

J. J. Mallorquí is with the Remote Sensing Laboratory, Signal Theory and Communications Department, Universitat Politècnica de Catalunya, 08034 Barcelona, Spain (e-mail: mallorqui@tsc.upc.edu).

R. Scheiber and A. Moreira are with the Microwaves and Radar Institute, German Aerospace Center (DLR), 82234 Oberpfaffenhofen, Germany (e-mail: Rolf.Scheiber@dlr.de; Alberto.Moreira@dlr.de).

Digital Object Identifier 10.1109/TGRS.2008.915758

0196-2892/$25.00 © 2008 IEEE

in the measurements of the real antenna position on the order of 1–5 cm. Several algorithms have been developed to estimate and correct RME, either the baseline error in an interferometric pair [20]–[23] or the individual error in an image [24], [25]. Section II-C addresses this topic.

Up to now, just a few publications related to airborne differential interferometry exist. In 1993, Gray and Farris-Manning [26] were able to measure the movement of a corner reflector with a precision on the order of some millimeters but measuring with respect to the field surrounding the corner. It was not until ten years later that the first airborne differential SAR interferogram of a large area was presented by Reigber and Scheiber [27], using a classical three-image DInSAR approach [28]. They measured some displacements in agricultural fields that might be related to the penetration depth of electromagnetic waves due to a different soil moisture and also obtained indication of water-level change in a swamp area. In 2004, de Macedo and Scheiber [29] presented some controlled experiments with three corner reflectors measured at both L- and C-band. In this case, relative and absolute measurements were shown, where the latter had an accuracy that was better than 1 cm. In 2004, Groot [30] reported the deformation of a dike after calibrating using the phase of several corner reflectors deployed in the scene. In addition, in 2004, Fornaro *et al.* [31] presented an X-band differential interferogram, where the images had been acquired with a temporal baseline of only a few minutes, so that no displacements were expected. In 2005, de Macedo *et al.* presented some preliminary results of a landslide [32]. Recently, Perna *et al.* [33] presented differential interferograms at X-band where the displacement of a corner reflector is retrieved.

This paper aims to describe, for the first time, the complete methodology and algorithms for processing a stack of images acquired by an airborne platform in order to retrieve the temporal evolution of the deformation in the observed scene. The processing chain to focus the data is described in Section II-E, where a detailed description is given in order to deal with the commented limitations. Section III starts revisiting the ADInSAR algorithm proposed by Berardino *et al.* [4], which has been used to obtain the deformation maps. In addition, the modifications needed in the ADInSAR processing to consider RME are expounded. Finally, Section IV presents results with data acquired by the Experimental SAR (E-SAR) system of the German Aerospace Center (DLR). Data were acquired the same day for 2.5 h. However, results show deformation in several agricultural fields, probably due to a change in soil moisture. The motion of one corner reflector that was moved intentionally during the experiment is also retrieved.

II. Motion Compensation

The real challenge in airborne repeat-pass InSAR processing, and particularly in DInSAR, is the accuracy of the MoCo. To reach millimeter accuracy at L-band, the phase accuracy must be better than 3°. This implies that a very accurate MoCo scheme must be used to properly deal with the nonlinear trajectory of the platform. Hence, one must consider the following two important limitations: the unknown topography in the scene under observation and the existence of RME.

Section II-A introduces several algorithms. The so-called extended chirp scaling (ECS) algorithm with integrated MoCo [34] is used for the efficient focusing of the raw data. However, in order to properly focus airborne SAR data, MoCo must consider topographic variations, as well as the dependence of the correction with the azimuth angle. Hence, there is a need for Topography- and Aperture-Dependent (TAD) MoCo algorithms. Three of such efficient algorithms are commented: the Sub-Aperture Topography- and Aperture-dependent (SATA) algorithm [17], the Precise Topography- and Aperture-dependent (PTA) algorithm [18], and the Frequency Division (FD) algorithm [19].

Concerning the algorithms to estimate RMEs, Section II-C comments several approaches. Four of them [20]–[23] are based on the spectral diversity or split-spectrum technique [35] applied in the azimuthal dimension. In this way, RMEs are estimated based on the azimuth coregistration offsets between two looks of an interferometric pair. In particular, the multisquint technique [23] uses several looks instead of only two as compared with the other approaches, resulting in an enhanced performance. Phase tracking of isolated or pointlike scatters techniques [24], [25] are an alternative to interferometric approaches, but they need a sufficient number of such targets to obtain reliable estimations.

A. TAD Motion Compensation

In order to properly focus a SAR image, the SAR processor performs a cross correlation with a 2-D reference function [36]–[38]. Under ideal conditions, i.e., when the platform follows a linear trajectory with a constant velocity, efficient processing considering the inherent space-variant effects of SAR imaging can be carried out in the spectral domain [34], [39]–[41]. Such conditions are met in a spaceborne scenario but not in an airborne one. The movement of the platform due to atmospheric turbulence introduces motion errors in the received raw data. If this movement is not considered, the final focused image will be severely degraded [42]–[44].

In order to take into account the motion of the platform, each target should be focused with a different 2-D reference function, increasing in this way the computation burden. Assuming that the motion of the aircraft has been recorded, commonly through differential global positioning (GPS) and inertial navigation systems [45], a MoCo approach within an efficient SAR processor is usually carried out [34], [44]. The main challenge is that the needed correction depends on the relative 3-D position between the target (topography) and the platform at every time instant (aperture), i.e., the phase history of the target and the location of the target information in the raw data are no longer hyperbolic. Therefore, exact focusing will be achieved, provided that the height of the target is known. This problem, coupled with the fact that the processing is space variant, has given raise to several TAD algorithms: SATA [17], PTA [18], and FD [19]. These algorithms rely on the two-step MoCo integrated in the ECS algorithm [34]. In this way, the two-step MoCo partially considers the space variance of

the impulse response, allowing accurate range cell migration correction. TAD algorithms deal with the remaining space-variant effects due to the topography and aperture by means of an azimuth block-processing approach, so that an accurately focused image can be obtained.

The image quality can be degraded if no TAD algorithm is used. The amount of degradation depends mainly on the topographic variations within the scene and the magnitude of the platform deviations [18]. The main effects are phase errors and the azimuth shift of the impulse response function (IRF). For large topographic variations and/or large track deviations, defocusing can also occur. Hence, these effects are just the result of constant, linear, and quadratic errors in the phase history of the target. Such errors will also result in a degraded interferogram, above all, in repeat-pass interferometric systems, where track deviations are not correlated. Therefore, in order to minimize phase and azimuth coregistration errors, a TAD algorithm should be used. These algorithms use an external digital elevation model (DEM), which must be back-geocoded to the slant range geometry, in order to properly consider the topography. The larger the error in the DEM, the larger the introduced phase and image distortions. In addition, the accuracy of each TAD algorithm should be considered (a comparison is presented in [46]). The selected algorithm to process the data of Section IV is SATA [17], since the external DEM used during MoCo has a low spatial resolution as compared to the azimuthal spatial resolution accommodation of SATA.

B. Interferometric Phase Content

An important key point is the information content of an interferogram after processing master and slave images with a TAD algorithm. The fact that MoCo is carried out using the external DEM implies that this information is introduced in the interferometric phase. However, interest lies in the unknown information, e.g., DEM errors or deformation. Consequently, the first step is to remove the information of the external DEM. This is carried out by subtracting the synthetic phase, which is computed using the external DEM and the reference tracks, from the generated interferogram. The remaining phase, called residual phase, contains the DEM error plus other contributions like deformation, atmospheric artifacts, and noise. It can be shown that the contribution of the DEM error to the synthetic phase is proportional to the real track deviations, so that, in the absence of the other contributions, the residual phase can be expressed as [46], [47]

$$\phi_{\text{residual}}(x,r) \approx k_z^{\text{real}}(x,r) h_{\text{err}}(x,r) \tag{1}$$

with

$$k_z^{\text{real}}(x,r) = -\frac{4\pi}{\lambda}\frac{B_\perp^{\text{real}}(x,r)}{r\sin\theta(r)} \tag{2}$$

where $B_\perp^{\text{real}}$ is the real perpendicular baseline, λ is the used wavelength, r is the range distance, x is the azimuth distance, and θ is the off-nadir look angle. Therefore, the subtraction of the synthetic phase is needed in order to remove the information introduced during MoCo. Otherwise, the content of the interferometric phase would be a mix between the external DEM, which is sensitive to the reference baseline (reference tracks), and the unknown topography, which is sensitive to the real baseline (real tracks). Equation (1) is important in differential interferometry, since it allows one to relate the residual phase linearly with the DEM error. Although it is a first-order approximation, it is quite accurate, as the DEM error is usually small. Note also that the larger the baseline gets with respect to the platform deviations, the more similar are the reference and real baselines.

C. Residual Motion Errors

The absolute positioning accuracy of current navigation systems using intertial navigation systems and differential GPS is about 1–5 cm. Therefore, the navigation data used during MoCo can have RMEs, resulting mainly in phase errors and azimuth impulse response shifts. Although such errors will not degrade significantly the high azimuthal resolution capability, some applications, like repeat-pass interferometry, differential interferometry, or very high resolution processing [24], can be strongly limited by them. Consequently, some procedure is needed to estimate the remaining trajectory deviations. Several algorithms have been proposed in the literature [20]–[25] of which the multisquint technique [23] has been used to estimate RME in the results of Section IV. This particular approach is based on the estimation of the azimuth coregistration offsets between multiple looks of an interferometric pair [35]. The coregistration offsets are related to the derivative of RME, so that after a proper scaling and integration, the time-varying baseline error can be retrieved. The estimated baseline error can be used to update the tracks of the slave image to reprocess it, so that afterward, both master and slave images will have the same RME of the master image, hence, canceling out after interferogram generation. The defocusing induced by the unknown RME of the master image can be neglected in interferometric applications.

In the case of having a stack of several images, different interferograms can be formed with the possibility of different images being master. In such a case, a first possibility is to select one of the images as master (from now on called I_0) so that the baseline error estimation using multisquint can be carried out with every interferogram formed between I_0 and each of the remaining images (slaves). Afterward, the slave tracks are updated with the estimates, ensuring that any combination between any image pair will result as RME-free, as all of them will have the same RME as image I_0. A second possibility is to estimate the baseline error of each individual interferogram, but this implies the reprocessing of each pair for every interferogram, resulting in an increase of the computation burden. Both approaches have been tested resulting in similar results [48]. The results of Section IV have been processed using the former approach, as expounded in Section II-E.

Other approaches to estimate RME are possible. In particular, the estimation of the individual RME using autofocus techniques by phase tracking of isolated or pointlike scatterers [24], [25] can be particularly attractive, above all considering

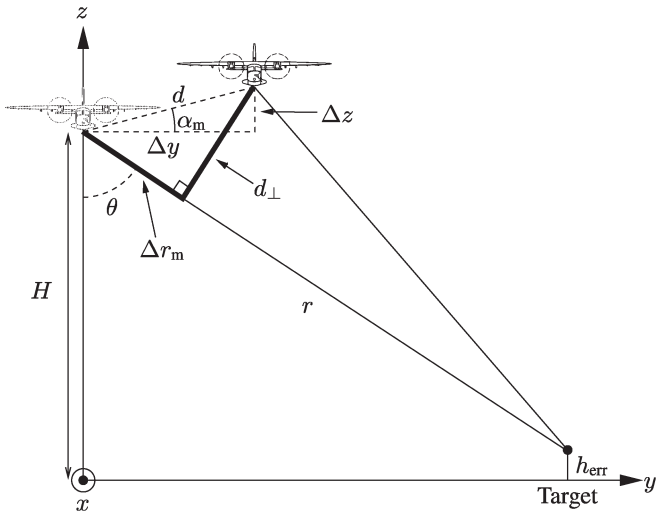

Fig. 1. Simplified sketch of MoCo geometry. $h_{\rm err}$ is the DEM error, Δr_m is the LOS motion error, d and α_m are the distance and the tilt angle, respectively, between real and reference positions, Δy is the horizontal displacement, Δz is the vertical displacement, and H the platform height above ground assumed during MoCo.

the potential coupling between the unknown topography and RME, as commented next.

D. Coupling Between Unknown Topography and RME

Up to now, the two main limitations, i.e., the unknown topography during MoCo and the estimation of RME (or baseline error), have been tackled separately. However, a coupling between them exists due to the fact that both have similar effects in the retrieved interferogram, mainly phase errors and azimuth coregistration offsets. This can become a problem if time-varying baseline error estimation techniques based on the estimation of coregistration offsets are used, as it is the case in the presented results. Therefore, it should be expected to retrieve a biased baseline error.

An analytical approach to analyze the problem is possible. Given the geometry of Fig. 1, the correction in line-of-sight (LOS) can be approximated by [44]

$$\Delta r_m \approx -d(t)\sin\left(\theta - \alpha_m(t)\right) \tag{3}$$

where $\alpha_m(t)$ is the tilt angle between real and reference positions, θ is the off-nadir look angle, and $d(t) = \sqrt{\Delta_y^2(t) + \Delta_z^2(t)}$, where $\Delta_y(t)$ is the horizontal deviation and $\Delta_z(t)$ is the vertical one. In order to retrieve the error as a function of the DEM error $h_{\rm err}$, a first-order approximation leads to

$$\Delta r_{m,h_{\rm err}}(t) = -\frac{d(t)\cos\left(\theta - \alpha_m(t)\right)}{r\sin\theta} h_{\rm err} = -\frac{d_\perp(t)}{r\sin\theta} h_{\rm err}. \tag{4}$$

A constant value of $d_\perp$ induces a phase offset through the phase history of the target, which, when combined with the slave image, results in (1), i.e., it results in the measurement of the unknown topography from the real antenna positions. However, a linear variation of $d_\perp$ through the synthetic aperture introduces an undesired azimuth shift of the impulse response.

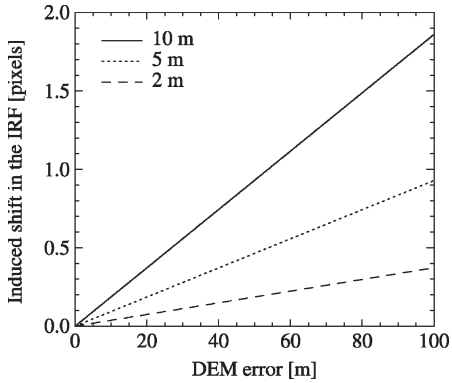

Fig. 2. Induced azimuth shift in the IRF for different total linear horizontal displacements along the synthetic aperture due to unknown topography for a target at midrange.

TABLE I
MAIN SYSTEM AND PROCESSING PARAMETERS

System PRF	400 Hz
Sampling frequency	100 MHz
Processed azimuth bandwidth	100 Hz
Processed range bandwidth	100 MHz
Wavelength	0.2305 m
Mid range	4582 m
Mean flight altitude	3219 m
Mean forward velocity	94.3 m/s
Processing squint angle	0°
Polarization	VV

Effectively, a linear phase error introduces the following shift in the IRF [18]:

$$\Delta x_{\rm shift} = -\frac{r_0}{v}\frac{\partial \Delta r_m}{\partial t} = -\frac{r_0}{v}\Delta v_m \tag{5}$$

where r_0 is the closest approach distance of the target and v is the forward velocity of the platform. Fig. 2 shows the azimuth shift in pixels as a function of the DEM error for three different total linear horizontal displacements along the synthetic aperture using the system parameters of Table I. Considering the high sensitivity of multisquint to estimate coregistration errors [49], the shift due to the unknown topography can reach critical values that will bias the baseline error estimation. In the case of multisquint, several spectral diversity phases are computed, which are aligned to the beam center geometry and added in order to reduce phase noise [23]. Although this alignment tends to cancel out the errors induced by the unknown topography, it cannot be expected that they will be completely removed, as the aircraft deviations are usually smooth through the synthetic aperture.

Fig. 3(a) shows the induced shift for a target at midrange all along the data take for two different acquisitions of the data of Section IV. A height error of 5 m has been assumed in both cases. The analysis has been carried out by fitting a line through $\Delta r_m(t)$ along the synthetic aperture length to retrieve Δv_m. Instead of considering a bandwidth of 100 Hz to compute the synthetic aperture length, a value of only 30 Hz has been used, as this is the used bandwidth of the looks during multisquint in the results of Section IV. The dashed line in Fig. 3 corresponds to a track with small deviations ($\Delta y < 6$ m), while the solid

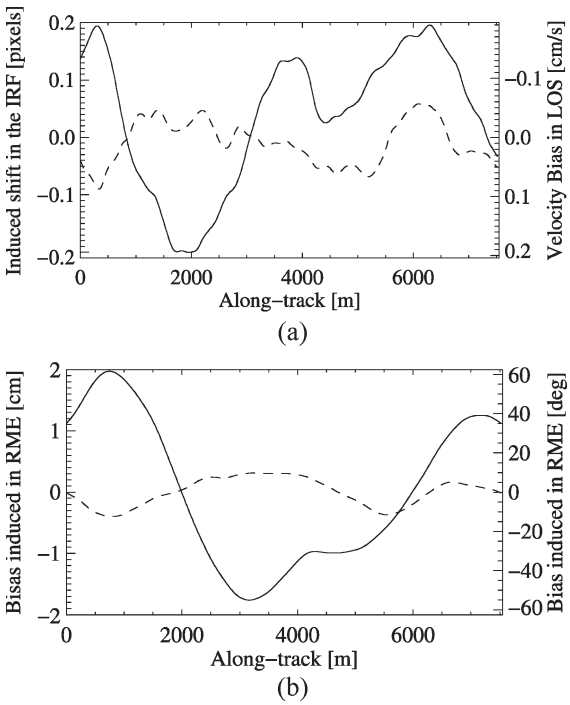

Fig. 3. (a) Induced azimuth shift in the IRF for a target at midrange and a height error of 5 m and (b) corresponding bias introduced in RME after integration (the phase error is computed at L-band). Track with (solid line) large and (dashed line) small deviations.

one corresponds to a track with large deviations ($\Delta y > 15$ m). The integration of these offsets given by [21]

$$\epsilon_{\mathrm{rme}}^{\mathrm{bias}}(x,r) = \int_0^x \frac{\Delta x_{\mathrm{shift}}(x')}{r} dx' + \mathcal{C} \tag{6}$$

leads to an error in the RME estimation $\epsilon_{\mathrm{rme}}^{\mathrm{bias}}(x,r)$, which will result in a bias when using multisquint. Fig. 3(b) shows this RME error for the same two track deviations as before. For the large track deviation, the induced error is almost ± 2 cm, hence, limiting the potential accuracy of airborne interferometry. The standard deviation of the shift of the IRF for all tracks of the data processed in Section IV is 0.06 pixels at midrange, assuming a height error of 5 m.

Concluding, the estimated baseline error might be biased when using multisquint, since the unknown topography can lead to an undesired shift of the IRF. Therefore, some procedure is needed to remove the remaining baseline error. In the presented case, this is done during the ADInSAR processing, as commented in Section III-B.

E. Implemented SAR Processing Chain

The processing chain used to focus the data shown in Section IV is shown in Fig. 4. The selected algorithms are ECS [34] to focus the raw data, SATA [17] to accommodate the topography and the aperture during MoCo, and multisquint [23] to estimate the time-varying baseline error.

In this case, the idea is to generate M interferograms from a set of N acquisitions. Instead of generating $M_0 = N - 1$

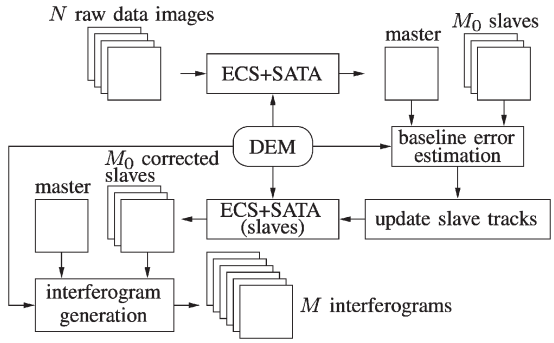

Fig. 4. Block diagram of the used processing chain. ECS stands for extended chirp scaling algorithm, while SATA stands for subaperture topography- and aperture-dependent MoCo algorithm.

interferograms, i.e., all slaves with respect to a master image I_0, several interferograms can be generated as carried out in several ADInSAR applications [4], [5]; for example, by selecting small baselines to maximize the coherence, so that M is usually greater than M_0. The differential processor will later on retrieve the deformation for each individual acquisition. Hence, the first step is to compute the reference tracks using the navigation data. By finding the best fit to all acquisition tracks, it is ensured that the reference tracks will be parallel and with the same azimuth image spacing [50], something that will ease the forthcoming interferometric steps. With the reference tracks and an external DEM, it is then possible to compute three different products in the slant range plane: the topographic height for the N images, M_0 coregistration error maps in range for each slave image with respect to the master image I_0, and M synthetic phases (for each interferogram) in the geometry of the master image I_0. Once the SAR focusing is carried out for each image using ECS and SATA, multisquint and the model-based integration proposed in [23] are used to estimate the baseline error for the first M_0 interferograms. Several iterations are performed with multisquint to improve the estimation. After the last iteration, constant and linear terms of the baseline error, which cannot be estimated by means of multisquint, are estimated using the external DEM, as also described in [23]. Note that, in order to carry out the multisquint estimation, it is first necessary to coregister the images in the range dimension, and also, the spectrum filtering can be applied if necessary. After multisquint, the slave images are processed again after updating their tracks with the full estimation of the baseline error. At this point, all the images have the RME of image I_0. Consequently, any combination between them will result in an RME-free interferogram, but note that, as already commented, a remaining baseline error might be present due to the coupling between the unknown topography and RME (see Section II-D).

It should be noted that the estimation of the baseline error for each of the M interferograms might be of interest when the temporal baseline or the geometric decorrelation increase with respect to image I_0. Doing so will yield a significant increase in the computation burden, but results will be more accurate in such scenarios. In the results to be presented, all images were acquired in the same day with a maximum baseline of 120 m with respect to the master image I_0, so that the

temporal coherence degradation is negligible, and spectrum filtering approaches solve the problem of spectral decorrelation.

The interferometric processor carries out the typical steps: range interpolation, spectrum filtering, interferogram generation, coherence estimation, phase unwrapping, and absolute calibration using a corner reflector. In this case, the external DEM has been used in some of these steps as follows.

1) Range coregistration: With the knowledge of the DEM and the master and slave reference tracks, it is possible to compute the coregistration offsets in range. Taking into account that the reference tracks are computed to be parallel, the images will be aligned in azimuth, implying that the time-consuming task of estimating the coregistration offsets is avoided.
2) Spectrum filtering: As expounded in [51], an efficient spectrum filtering can be carried out with the knowledge of the topography. By subtracting the synthetic phase computed with the DEM to the master and slave images, the spectrum is basebanded, easing, in this way, the filtering of the common part with a simple low-pass filter.
3) Coherence estimation: The bias introduced in the coherence due to the topographic phase can be reduced by subtracting again the synthetic phase to one of the images prior to coherence computation.
4) Phase unwrapping: The reduction of fringes using the synthetic phase is a standard procedure whenever a DEM is available. However, in the described scheme, the subtraction of the synthetic phase is mandatory, as the valuable interferometric information is stored in the residual phase.

Once the interferometric processing of all M interferograms is finished, the data are prepared to be processed by the ADInSAR processor.

III. Advanced Airborne DInSAR

There are several techniques to retrieve the temporal evolution of the deformation in a stack of images [1]–[6]. The differential technique presented by Berardino *et al.* [4] has been selected to process the data of Section IV. In the following, this technique is briefly described for completeness, while the modifications in order to deal with airborne data are detailed in Section III-B.

A. Small Baseline Technique (SBAS)

The SBAS [4] is based on the use of small baseline interferometric pairs to maximize the number of coherent points. This technique is well suited to DInSAR when not only permanent scatterers are being analyzed but also distributed targets with enough coherence between the acquisitions. Therefore, a multilook is generally carried out to the interferograms, with a size equal to the coherence estimation window. Note that high-resolution results can be obtained with additional steps, as detailed in [6].

Prior to starting the algorithm, it is assumed that the residual phases (from now on, called differential phases, as the external DEM has been subtracted) have been unwrapped and calibrated

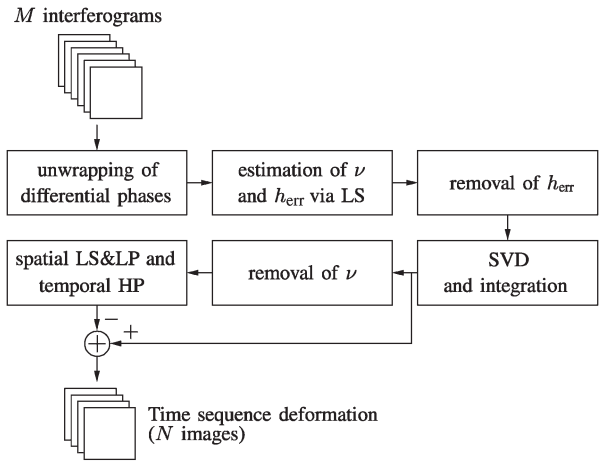

Fig. 5. Block diagram of the implemented ADInSAR algorithm. SVD stands for singular-value decomposition, LS for least squares (estimation), and LP and HP for low- and high-pass (filtering), respectively.

with respect to one pixel whose deformation is known (usually, a highly coherent pixel without deformation). This allows one to make a pixel-by-pixel temporal analysis. The block diagram of the implemented algorithm is shown in Fig. 5.

Let

$$\phi^{\mathrm{T}} = [\phi(t_1), \ldots, \phi(t_{N-1})] \tag{7}$$

be the vector of the $N-1$ unknown phase values associated with the deformation of the considered pixel and

$$\phi_{\mathrm{diff}}^{\mathrm{T}} = [\phi_{\mathrm{diff},1}, \ldots, \phi_{\mathrm{diff},M}] \tag{8}$$

be the vector of the M known values of the computed differential interferograms. Two index vectors are defined

$$\begin{aligned} \mathrm{IE} &= [\mathrm{IE}_1, \ldots, \mathrm{IE}_M] \\ \mathrm{IS} &= [\mathrm{IS}_1, \ldots, \mathrm{IS}_M] \end{aligned} \tag{9}$$

which correspond to the acquisition time indexes associated with the image pairs used for the interferogram generation. It is also assumed that the master (IE) and slave (IS) images are chronologically ordered, i.e., $\mathrm{IS}_j > \mathrm{IE}_j, \forall j = 1, \ldots, M$.[1] This results in

$$\phi_{\mathrm{diff},j} = \phi(t_{\mathrm{IE}_j}) - \phi(t_{\mathrm{IS}_j}) \qquad \forall j = 1, \ldots, M. \tag{10}$$

Given two SAR images with acquisition times t_A and t_B ($t_A < t_B$), the differential phase after subtracting the external DEM is given by

$$\begin{aligned} \phi_{\mathrm{diff},j} &= \phi(t_A, x, r) - \phi(t_B, x, r) \\ &\approx \frac{4\pi}{\lambda} \cdot [d_{\mathrm{los}}(t_A, x, r) - d_{\mathrm{los}}(t_B, x, r)] + k_z^{\mathrm{real}} \cdot h_{\mathrm{err}} \\ &\quad + \phi_{\mathrm{err}}(t_A, x, r) - \phi_{\mathrm{err}}(t_B, x, r) + \Delta n_j \\ &\quad \forall j = 1, \ldots, M \end{aligned} \tag{11}$$

[1]Note that, in the original reference [4], they consider the opposite, i.e., $\mathrm{IE}_j > \mathrm{IS}_j, \forall j = 1, \ldots, M$.

where $d_{\text{los}}(\cdot)$ represents the displacement in LOS at every time instant. Note that the real tracks are used to compute k_z^{real}, as commented in Section II-B. The h_{err} term accounts for possible phase artifacts due to an error in the external DEM. The third term in (11), represented by $\phi_{\text{err}}(t_A, x, r) - \phi_{\text{err}}(t_B, x, r)$, accounts for possible RMEs, which might have not been properly estimated and corrected, and for atmospheric artifacts (atmospheric phase component). Finally, the term Δn_j represents the phase noise due to all sources of decorrelation.

The major difficulty in differential interferometry lies in the unwrapping of the differential phases. Even if an external DEM is used to remove the topographic component, errors in this DEM, atmospheric artifacts, RMEs, or even the displacement to estimate itself, can result in a wrapped differential phase. The unwrapping operation is performed to each differential interferogram, but only the pixels that have a mean coherence higher than a certain threshold are used. Usually, in differential applications, a sparse grid has to be unwrapped. Berardino *et al.* [4] propose to use the approach presented in [52] to carry out this phase unwrapping. Since the data presented in Section IV were acquired in only one day and are very coherent, the conventional region-growing algorithm with weighted least mean squares has been used [53].

After phase unwrapping, the linear component of the deformation and any possible DEM error are estimated via a least squares (LS) solution. Therefore, the following system of equations can be formed for each pixel:

$$\mathbf{A}\mathbf{p} = \phi_{\text{diff}} \tag{12}$$

with

$$\mathbf{A} = \begin{bmatrix} \frac{4\pi}{\lambda}\Delta t_1 & k_{z,1}^{\text{real}} \\ \vdots & \vdots \\ \frac{4\pi}{\lambda}\Delta t_M & k_{z,M}^{\text{real}} \end{bmatrix} \quad \begin{matrix} \Delta t_j = t_{\text{IS}_j} - t_{\text{IE}_j} \\ \forall j = 1, \ldots, M \end{matrix} \tag{13}$$

$$\mathbf{p} = \begin{bmatrix} \nu \\ h_{\text{err}} \end{bmatrix} \tag{14}$$

$$\phi_{\text{diff}} = \begin{bmatrix} \phi_{\text{diff},1} \\ \vdots \\ \phi_{\text{diff},M} \end{bmatrix} \tag{15}$$

where ν is the mean deformation velocity. The LS solution is given by

$$\mathbf{p} = (\mathbf{A}^{\text{T}}\mathbf{A})^{-1}\mathbf{A}^{\text{T}}\phi_{\text{diff}}. \tag{16}$$

Once the DEM error h_{err} and the mean deformation velocity ν have been estimated, the DEM error is subtracted to each of the differential interferograms modulo 2π, leading to a fringe-rate reduction of the differential phase. All differential interferograms might be unwrapped again, but in the presented case, this second phase-unwrapping step has been omitted, given the good coherence of the whole data set. Indeed, in [4], both the DEM error and the mean deformation velocity are subtracted, so that the differential interferograms are unwrapped again, and after phase unwrapping, ν is added. The next step is to find the deformation for each image ϕ, which is solved via singular value decomposition (SVD). As recommended in [4], the mean phase velocity between time-adjacent acquisitions is used in the SVD, instead of the individual phases. A final integration step yields the desired solution $\phi(t_i)$.

The problem with spaceborne data is that the estimated displacements are affected by atmospheric artifacts. Berardino *et al.* [4] propose to perform a filtering operation to the estimated $\phi(t_i)$, which is derived from the permanent scatterers approach [1], [2]. It is based on the fact that the atmospheric signal phase component is characterized by a high spatial correlation but exhibits a significantly low temporal correlation. Accordingly, the undesired atmospheric phase component can be estimated after the SVD as follows. First, the low-pass component of the deformation signal already estimated via (16) is removed. Afterward, the atmospheric phase component is detected as the result of the cascade of a low-pass filtering step, performed in the 2-D spatial domain (i.e., azimuth and range), and a high-pass (HP) filtering operation with respect to the time variable. Once the atmospheric phase component has been evaluated, it is finally subtracted from the estimated phase signal.

However, in the airborne case, one has to further deal with the presence of RMEs, which might have not been properly estimated. In the next section, a modified filtering approach to remove them is proposed.

B. Modifications in the Airborne Case

Besides using the real baseline instead of the reference one, the main difference arises due to the existence of RMEs. The fact that RMEs might have not been properly estimated and corrected (as noted in Section II-D) implies that some kind of filtering should be carried out to remove them from the differential interferograms. Furthermore, the atmospheric component should not be neglected, even at L-band [3].

This filtering can be carried out at the same point as when the atmosphere is estimated in the spaceborne case, i.e., after the SVD estimation and having subtracted the previously estimated mean deformation velocity. In theory, only the nonlinear deformation should remain, but the presence of baseline errors and atmospheric artifacts must be considered. Their contribution can be described as

$$\begin{aligned} \phi_{\text{err}}(t_i, x, r) &= \frac{4\pi}{\lambda}\epsilon_{\text{rme}} + \frac{4\pi}{\lambda}\epsilon_{\text{atm}} \\ &= \frac{4\pi}{\lambda} \cdot (\epsilon_y(x)\sin\theta(r) - \epsilon_z(x)\cos\theta(r)) \\ &\quad + \frac{4\pi}{\lambda}10^{-6} \cdot \int_0^H \frac{N(x, r, h)}{\cos\theta(r)} dh \end{aligned} \tag{17}$$

where the baseline error ϵ_{rme} is just the projection in LOS of the individual unknown horizontal ϵ_y and vertical ϵ_z displacements and N is the scaled-up refractivity equal to $N = (n-1) \cdot 10^6$, where n is the refractive index of the medium. Note that the slant atmospheric delay is inversely proportional to the cosine of the look angle [3] and has a high spatial correlation. An important approximation in (17) is that a 0° squint angle is

being assumed. In a squinted geometry, an azimuth phase ramp would be present, which, depending on the coregistration error due to the unknown topography, could introduce important phase errors [35]. However, the E-SAR system has a large azimuth beamwidth at L-band ($\sim 18^\circ$), so that a 0° processing squint angle can be selected without a significant loss in the signal-to-noise ratio. A further approximation is the assumption that the nonlinear deformation is small enough not to bias the refined estimation of the baseline error. Finally, it should be stressed again that the error contribution of baseline errors and atmosphere in each of the $N-1$ images of the deformation sequence is a differential error between the corresponding slave image and master image I_0.

A possible approach to estimate the two contributions would be to first estimate the baseline error from each image of the deformation sequence using an LS-estimation approach, subtract them from the data, and then filter the atmospheric component by means of a large low-pass filter. Therefore, an LS estimation is performed for every azimuth position x to obtain the remaining baseline error using all N_r samples in range. Using the same model as in [23] yields

$$\epsilon_{yz} = (\mathbf{A}^{\mathrm{T}}\mathbf{A})^{-1}\mathbf{A}\boldsymbol{\delta\phi} \tag{18}$$

with

$$\mathbf{A} = \begin{bmatrix} \sin\theta_1 & -\cos\theta_1 \\ \vdots & \vdots \\ \sin\theta_{N_r} & -\cos\theta_{N_r} \end{bmatrix} \tag{19}$$

$$\boldsymbol{\epsilon}_{yz} = \begin{bmatrix} \epsilon_y \\ \epsilon_z \end{bmatrix} \tag{20}$$

$$\boldsymbol{\delta\phi} = \frac{\lambda}{4\pi}[\delta\phi_1, \ldots, \delta\phi_{N_r}] \tag{21}$$

where $\boldsymbol{\delta\phi}$ corresponds to the phase values at a given azimuth position of an entire range line and $\theta_1, \ldots, \theta_{N_r}$ correspond to the off-nadir look angle at every range bin. $\boldsymbol{\delta\phi}$ contains the projection in LOS of the baseline error, together with the atmospheric component, the nonlinear motion of the deformation, and noise. Therefore, the LS estimation obtains the individual components ϵ_y and ϵ_z of the remaining baseline error. Since all pixels are assumed to have an acceptable coherence level, no weighting is applied in the LS estimation. After subtracting the remaining baseline error to the differential interferogram, a large low-pass filtering can be carried out. In the airborne geometry, the look angle changes considerably along the scene (ca. 25°–55°). Therefore, in order to consider the look-angle dependence, data should be first multiplied by $\cos\theta(r)$. Now, the large low-pass filter can be applied to the image to retrieve the atmospheric component. Finally, the estimated atmospheric component is subtracted from the data after dividing it by $\cos\theta(r)$. After the correction of baseline errors and atmosphere, a further HP filtering in time reduces the influence of these two effects, which are subtracted from the deformation series in the last step of the algorithm.

The estimation of the DEM error h_{err} and the mean velocity ν via LS estimation performs better, the larger the number of independent acquisitions. Since in the presented case only $N = 14$ independent acquisitions are available, the estimated h_{err} and ν might be biased. If this biased ν is subtracted before the refined estimation of the baseline error (as shown in Fig. 5), then the refinement will not perform accurately. Therefore, in a first iteration, ν should not be subtracted before the LS estimation. Once the refinement has been performed, a second iteration can be carried out, but, this time, correcting the M interferograms with the refined estimates. The atmospheric component might be also considered here, although, in the presented results, only the baseline error has been taken into account. The improvement in the results with the second iteration is significant, as shown in next the section. Obviously, here, it is assumed that the deformation will not bias this refined estimation in the first iteration, something that is valid as long as the deformation is located in a small area in range and is not much larger than the baseline error.

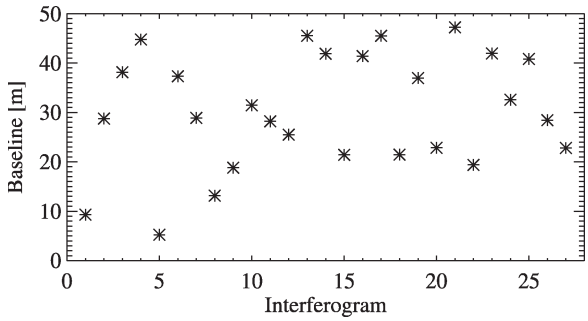

Fig. 6. Baseline distribution for the selected interferograms.

IV. Experimental Results

A total of 14 images were acquired at L-band by the E-SAR system of DLR during a time span of 2.5 h (from 11 A.M. until 1:24 P.M. with $\sim$11 min between each acquisition) in the test site of Oberpfaffenhofen, Germany. The data acquisition took place on May 11, 1998 in order to carry out the first tomographic experiment with a SAR system [54]. This same data set has been used to analyze the performance and limitations of ADInSAR techniques when working with airborne data. With 14 images, up to 91 interferograms can be formed. However, a maximum baseline of 50 m has been imposed in order to keep a large number of coherent points without much spectral filtering (better range resolution), resulting in a total number of 27 interferograms (see the baseline distribution in Fig. 6). Nevertheless, larger baselines lead to a similar result, as reported in [48], where, in that case, 51 interferograms were generated by imposing a maximum baseline of 90 m. Fig. 7 shows the reflectivity image of the observed scene, while Fig. 8 shows a detail with the location of the 11 corner reflectors.

The multilook applied to the interferograms and the window for coherence estimation are of 4 pixels $\times$ 4 pixels, so that the image spacing after the multilook is about 6 m $\times$ 6 m. Those pixels having a coherence larger than 0.8 in at least 50% of the interferograms have been selected. In addition, the mask generated by the region-growing algorithm for each interferogram has been used to discard pixels not properly unwrapped. Fig. 9(a) shows the mean coherence of all 27 interferograms,

Fig. 7. Reflectivity image of the observed scene. Scene dimensions: 7 × 2 km (azimuth × range). Image resolution: 1.3 × 1.9 m.

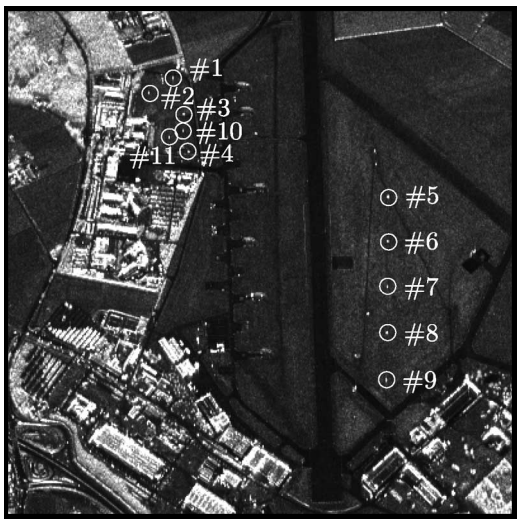

Fig. 8. Detail of the reflectivity image showing the location of the 11 corner reflectors.

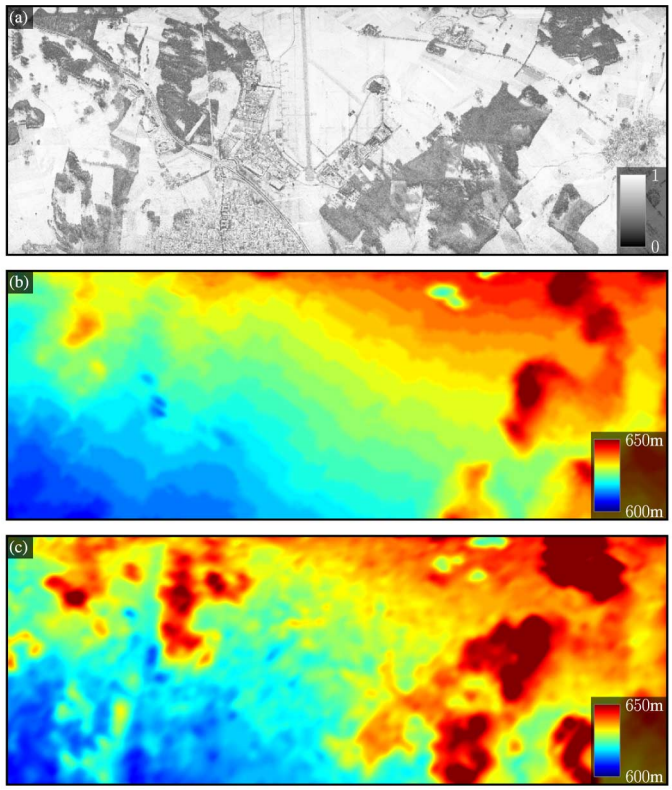

Fig. 9. (a) Mean coherence for all 27 interferograms, and DEMs from (b) MagicMaps and (c) SRTM used during the processing. Note that (b) is indeed a DTM, while (c) includes the height of the vegetation.

while Fig. 9(b) and (c) shows the two different DEMs used during MoCo. The reason to use two different DEMs is to validate the proposed processing chain, so that the retrieved deformation maps are the same independently of the used DEM. The first DEM [a digital terrain model (DTM)] is provided by MagicMaps GmbH as a commercial product and has a nominal resolution of 50 × 50 m (http://www.magicmaps.de/). The second is a C-band Shuttle Radar Topography Mission (SRTM) DEM with a nominal resolution of 90 × 90 m (http://www.jpl.nasa.gov/srtm/). It will be shown that, except for the DEM error, the estimated deformation and baseline errors are basically the same.

After subtracting the external DEM to each interferogram, the differential interferograms have been unwrapped and calibrated using corner reflector #6 (see Fig. 8). Once the LS estimation is applied to each selected pixel, the DEM error and the mean deformation velocity maps are obtained. Fig. 10(a) and (b) shows the DEM error for the two DEMs, where it can be noted that the height of some buildings has been properly retrieved, as one of the interferograms with a smaller baseline supported the phase unwrapping of the others. Fig. 10(c) shows the refined DEM after adding the error to the original DEM. The output for both refined DEMs is the same, with a standard deviation in the height difference of only 12 cm after subtracting an azimuth and a range linear component. The linear component in range was the larger one, with a

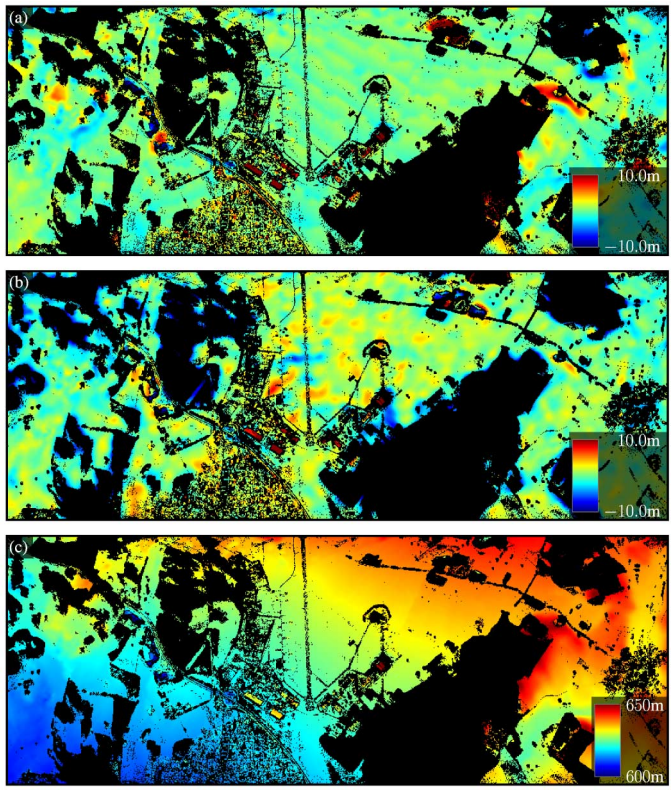

Fig. 10. Retrieved DEM error derived from the DEM provided by (a) MagicMaps GmbH and (b) SRTM and (c) refined DEM. Masked values in black.

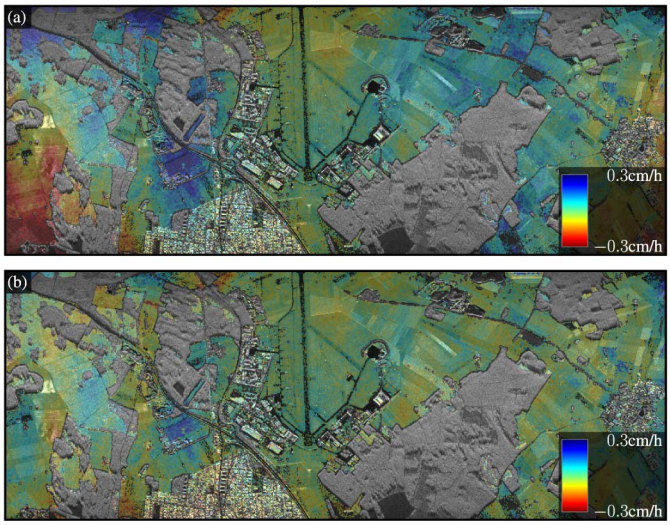

Fig. 11. Retrieved (a) mean deformation velocity in LOS with overlayed reflectivity and (b) mean deformation velocity in LOS after a second iteration using the refined correction of the baseline error.

variation in range of about ± 1 m. In addition, a mean offset of 0.28 m was present. These linear and constant components come from the difference in the original DEMs. Indeed, constant and linear terms of the baseline error are estimated using the external DEM, so that their accuracy depends mainly on the accuracy of the external DEM. In order to test this hypothesis, the data processed with the SRTM DEM were reprocessed with the ADInSAR processor but using the constant and linear terms of the baseline error estimated with the MagicMaps DEM. As expected, linear trends disappeared, and only a mean offset of 9 cm remained, being the standard deviation between both refined DEMs of 10 cm.

A third approach was carried out by applying MoCo, assuming a constant reference height for the whole image, i.e., no topography accommodation was applied during the focusing. Since the scene under study has very low topography, the focused images were not noticeably degraded. In this case, constant and linear terms of the baseline error obtained with MagicMaps DEM were used. The standard deviation in the difference between the refined DEM, as compared to when the processing is carried out with MagicMaps DEM, is 0.62 m, with a mean of 0.13 m. It should be noted that, although in the presented scenario not considering the topography results in a fairly good estimation, in scenes with more topography, a TAD algorithm becomes mandatory to reduce the coupling between the unknown topography and RMEs and to improve the quality of the interferogram.

Fig. 11(a) shows the mean deformation velocity map in LOS. In order to improve the estimation of the mean deformation map and the DEM error, a second iteration with the ADInSAR processor was carried out. In this second case, the refined estimation of the baseline error after the SVD was used as commented in Section III-B. The refined result of the mean deformation velocity is shown in Fig. 11(b).

Concerning the deformation results, some motion is measured in corner reflector #11, which was indeed moved intentionally during the data take. The second mobile corner

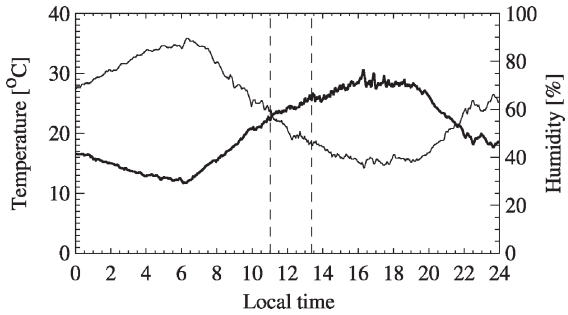

Fig. 12. (Solid thick line) Temperature and (solid thin line) humidity measured by the meteorological station located inside DLR facilities at Oberpfaffenhofen the day of the data take. The vertical dashed lines indicate the beginning and the end of the data take.

reflector (#10) also shows some movement, although it was not moved during the experiment. Unexpectedly, several geometrical shapes are observed all around the image, and they do not seem to be a processing artifact. In fact, it can be noted how these shapes correlate well with the shapes of the agricultural fields. Hence, some deformation is indeed being observed. Some fields show a raise and others a downfall of the phase center. The most plausible explanation for these effects is that the soil moisture content changed, similarly as reported in [11], [27], and [55]. In the case of a raise of the phase center, the soil moisture might have increased during the experiment due to dew, reducing, in this way, the penetration depth of the electromagnetic waves, or maybe due to a raise of the vegetation itself (note that irrigation is not usual in the area under study). On the other hand, the downfall of the phase center in some fields might occur due to evaporation of water, reducing the soil moisture and, hence, increasing the penetration depth. Fig. 12 shows the temperature and humidity measured by the meteorological station located inside DLR facilities at Oberpfaffenhofen the day of the data take. The temperature raised from 22.1 °C at 11 A.M. to 25.6 °C at 1:24 P.M., while the humidity reduced from 59.6% to 45.4%.

After subtracting the DEM error h_{err}, the SVD approach is applied to obtain the time-sequence deformation of images. Then, the filtering commented in Section III-B is carried out to estimate the remaining baseline error and the atmosphere. The estimated atmospheric component is very small in this particular data set, with a standard deviation of only 0.7 mm in all images. Fig. 13 shows the refined baseline estimation for two different tracks and for both DEMs. It can be noted how the estimations for the two DEMs differ, but the final refined ones are fairly the same. The main difference is an offset, which again is due to errors in the original DEMs. The standard deviation in the baseline error difference between processing with the two DEMs is about 1.1 mm.

Fig. 14(a) shows the deformation evolution for the corner reflectors. Diamonds correspond to the corners next to the runway (corners #5–#9), squares to the fixed ones on the left (corners #1–#4), and stars to the mobile ones (corners #10 and #11). The mobile corner reflector that shows a larger motion corresponds to the one moved intentionally during the experiment (corner #11). No filter in the time domain was applied in this case to avoid filtering the nonlinear motion of the mobile

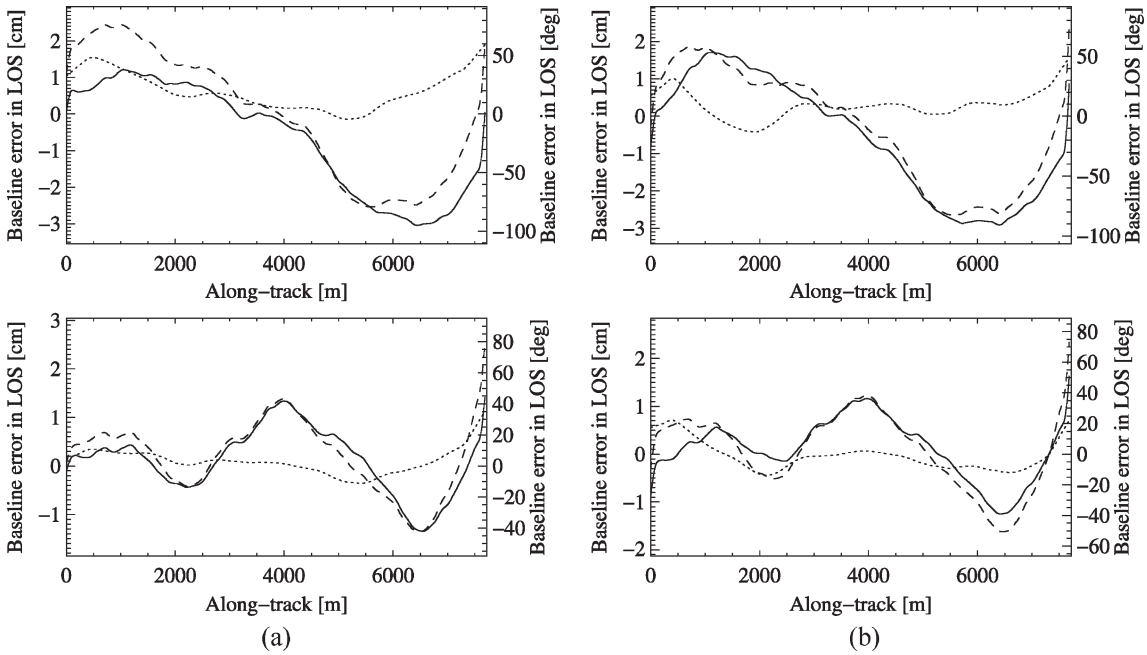

Fig. 13. Estimated baseline error in LOS with (solid line) multisquint, (dotted line) during the ADInSAR processing, and (dashed line) refined baseline error after adding the previous two. Track with (top) large and (bottom) small deviations. For (a) MagicMaps DEM and (b) SRTM DEM.

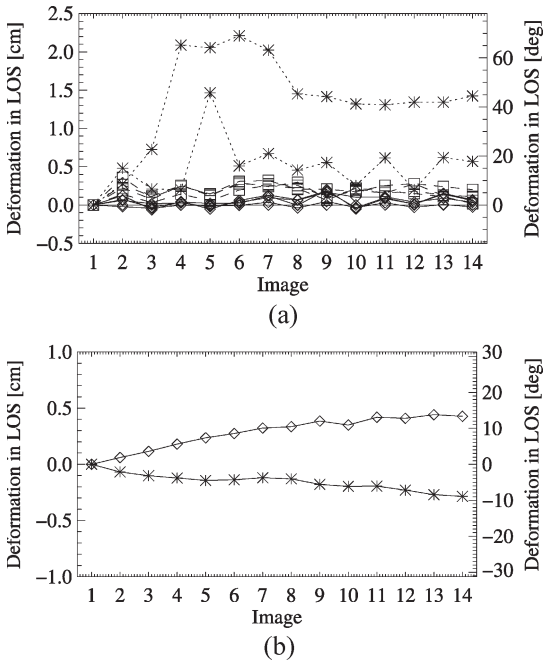

Fig. 14. (a) Deformation evolution in LOS for all corner reflectors without filter in the time domain. The corners are as follows: (squares) corners #1–#4, (diamonds) corners #5–#9, and (stars) corners #10 and #11. (b) Deformation in two different fields: (diamonds) upraise and (stars) downfall of the phase center. Their location is shown in Fig. 16.

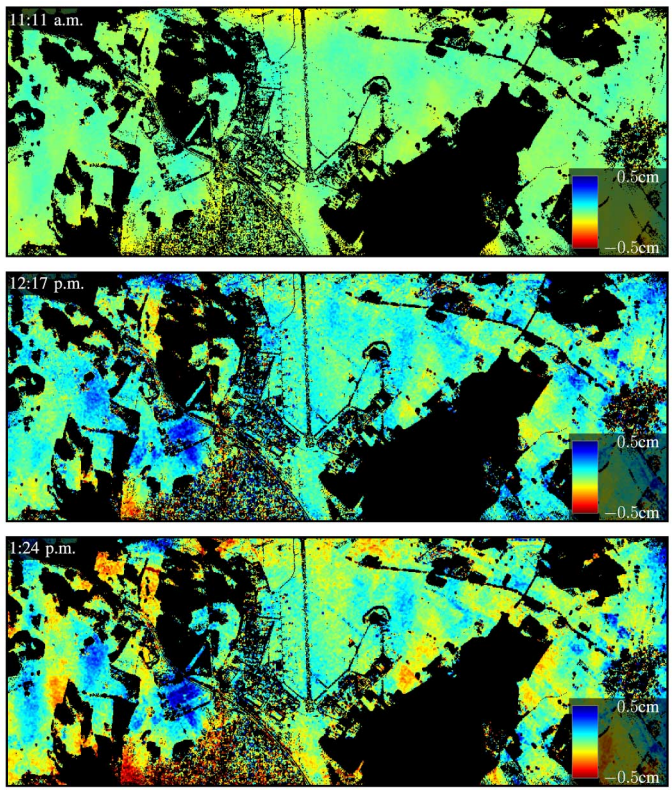

Fig. 15. Three images of the deformation evolution in LOS, with the local time of each image acquisition on the top-left corner. Acquisition started at 11 A.M. and finished at 1:24 P.M.

corner reflector. Fig. 14(b) shows the deformation evolution of two pixels located in two different fields. One is showing an upraise of the phase center, while the second shows a downfall. Unfortunately, none of these results can be validated, since no *in situ* measurements are available.

Fig. 15 shows the deformation at some time instants (note that the acquisition started at 11 A.M. and finished at 1:24 P.M.), where the change in phase center of the fields can be clearly observed. Fig. 16 shows the estimated mean deformation, where, again, it can be noted how the detected deformation areas correlate well with the shape of agricultural fields. The standard deviation in the difference between the mean displacement maps obtained when processing with the two different DEMs

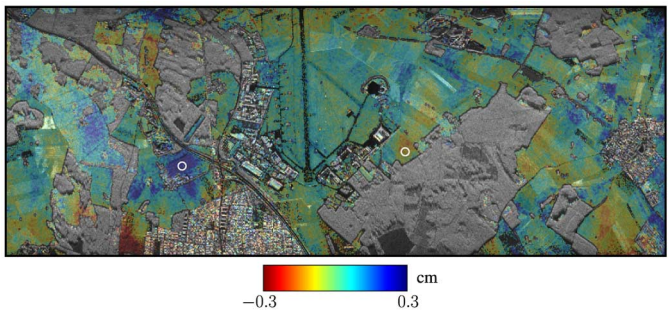

Fig. 16. Estimated mean deformation with overlayed reflectivity (from 11 A.M. to 1:24 P.M.). The white circles indicate the location of the pixels whose deformation is shown in Fig. 14(b).

is of 0.7 mm, but it reduces to 0.3 mm when using the same estimation of constant and linear terms of the baseline error.

Finally, note that the magnitude of the measured deformations is around $\lambda/20$. Such good accuracy is possible due to the short time span between acquisitions, allowing an exceptionally good coherence between them.

V. Conclusion

This paper has shown the potential of airborne platforms to retrieve differential interferometric products, presenting results for the first time with a large stack of images and ADInSAR techniques. The processing strategy to focus the data has been expounded, emphasizing the limitations in airborne systems. In this sense, RMEs are the main limitation. The multisquint technique used to estimate the baseline error can lead to a bias as a consequence of the undesired shift of the IRF due to errors in the external DEM. Therefore, a solution is proposed during the ADInSAR processing to estimate the remaining baseline error. To test the proposed approach, two different external DEMs have been used for the processing. The retrieved deformation maps and refined baseline errors are basically the same, and the minor differences are due to the accuracy of the original DEMs. The use of an external DEM is necessary in order to apply accurate MoCo, as well as being of great help in several steps of the interferometric processing. Furthermore, it is also used to estimate constant and linear terms of the baseline error, as described in [23].

Besides the motion detection of a corner reflector that was moved intentionally, it has been possible to detect some deformation of just a few millimeters in several agricultural fields, probably due to a change in soil moisture or vegetation vitality during the data take. The high correlation between the shapes of the deformation areas and the agricultural fields allows one to validate the presented results. Unfortunately, no *in situ* measurements are available. Ideally, a proper validation of the proposed techniques should be carried out by performing a campaign over a more controlled scenario.

Future work will address the use of approaches like [24] and [25] to estimate RME in each individual image, instead of the baseline error. In this way, the estimation is not affected by the shift of the IRF due to the unknown topography during MoCo. Consequently, the RME in the interferograms will be small, increasing the reliability of the proposed approach. Finally, the operational interferometric data processing chain of the E-SAR system is being expanded to include ADInSAR processing capability.

Acknowledgment

The authors would like to thank the anonymous reviewers for their comments and suggestions.

References

[1] A. Ferretti, C. Prati, and F. Rocca, "Nonlinear subsidence rate estimation using permanent scatterers in differential SAR interferometry," *IEEE Trans. Geosci. Remote Sens.*, vol. 38, no. 5, pp. 2202–2212, Sep. 2000.

[2] A. Ferretti, C. Prati, and F. Rocca, "Permanent scatterers in SAR interferometry," *IEEE Trans. Geosci. Remote Sens.*, vol. 39, no. 1, pp. 8–30, Jan. 2001.

[3] R. F. Hanssen, *Radar Interferometry. Data Interpretation and Error Analysis*. Dordrecht, The Netherlands: Kluwer, 2001.

[4] P. Berardino, G. Fornaro, R. Lanari, and E. Sansosti, "A new algorithm for surface deformation monitoring based on small baseline differential SAR interferograms," *IEEE Trans. Geosci. Remote Sens.*, vol. 40, no. 11, pp. 2375–2383, Nov. 2002.

[5] O. Mora, J. J. Mallorqui, and A. Broquetas, "Linear and nonlinear terrain deformation maps from a reduced set of interferometric SAR images," *IEEE Trans. Geosci. Remote Sens.*, vol. 41, no. 10, pp. 2243–2253, Oct. 2003.

[6] R. Lanari, O. Mora, M. Manunta, J. J. Mallorqui, P. Berardino, and E. Sansosti, "A small-baseline approach for investigating deformations on full-resolution differential SAR interferograms," *IEEE Trans. Geosci. Remote Sens.*, vol. 42, no. 7, pp. 1377–1386, Jul. 2004.

[7] D. Perissin and F. Rocca, "High-accuracy urban DEM using permanent scatterers," *IEEE Trans. Geosci. Remote Sens.*, vol. 44, no. 11, pp. 3338–3347, Nov. 2006.

[8] D. Perissin, C. Prati, M. E. Engdahl, and Y. L. Desnos, "Validating the SAR wavenumber shift principle with the ERS–Envisat PS coherent combination," *IEEE Trans. Geosci. Remote Sens.*, vol. 44, no. 9, pp. 2343–2351, Sep. 2006.

[9] A. Ferretti, G. Savio, R. Barzaghi, A. Borghi, S. Musazzi, F. Novali, C. Prati, and F. Rocca, "Submillimeter accuracy of InSAR time series: Experimental validation," *IEEE Trans. Geosci. Remote Sens.*, vol. 45, no. 5, pp. 1142–1153, May 2007.

[10] F. Chaabane, A. Avallone, F. Tupin, P. Briole, and H. Maître, "A multitemporal method for correction of tropospheric effects in differential SAR interferometry: Application to the Gulf of Corinth earthquake," *IEEE Trans. Geosci. Remote Sens.*, vol. 45, no. 6, pp. 1605–1615, Jun. 2007.

[11] A. K. Gabriel, R. M. Goldstein, and H. A. Zebker, "Mapping small elevation changes over large areas: Differential radar interferometry," *J. Geophys. Res.*, vol. 94, no. B7, pp. 9183–9191, 1989.

[12] D. Massonnet, M. Rossi, C. Carmona, F. Adragna, G. Peltzer, K. Fiegl, and T. Rabaute, "The displacement field of the Landers earthquake mapped by radar interferometry," *Nature*, vol. 364, no. 6433, pp. 138–142, Jul. 1993.

[13] R. Horn, "The DLR airborne SAR project E-SAR," in *Proc. IGARSS*, Lincoln, NE, May 27–31, 1996, vol. 3, pp. 1624–1628.

[14] Y. Kim, Y. Lou, J. van Zyl, L. Maldonado, T. Miller, T. Sato, and W. Skotnicki, "NASA/JPL airborne three-frequency polarimetric/interferometric SAR system," in *Proc. IGARSS*, Lincoln, NE, May 27–31, 1996, vol. 3, pp. 1612–1614.

[15] S. Uratsuka, M. Satake, T. Kobayashi, T. Umehara, A. Nadai, H. Maeno, H. Masuko, and M. Shimada, "High-resolution dual-bands interferometric and polarimetric airborne SAR (π-SAR) and its applications," in *Proc. IGARSS*, Toronto, ON, Canada, Jun. 24–28, 2002, vol. 3, pp. 1720–1722.

[16] E. Christensen, N. Skou, J. Dall, K. W. Woelders, J. Jorgensen, J. Granholm, and S. Madsen, "EMISAR: An absolutely calibrated polarimetric L- and C-band SAR," *IEEE Trans. Geosci. Remote Sens.*, vol. 36, no. 6, pp. 1852–1865, Nov. 1998.

[17] P. Prats, A. Reigber, and J. J. Mallorqui, "Topography-dependent motion compensation for repeat-pass interferometric SAR systems," *IEEE Geosci. Remote Sens. Lett.*, vol. 2, no. 2, pp. 206–210, Apr. 2005.

[18] K. A. C. de Macedo and R. Scheiber, "Precise topography- and aperture-dependent motion compensation for airborne SAR," *IEEE Geosci. Remote Sens. Lett.*, vol. 2, no. 2, pp. 172–176, Apr. 2005.

[19] X. Zheng, W. Yu, and Z. Li, "A novel algorithm for wide beam SAR motion compensation based on frequency division," in *Proc. IGARSS*, Denver, CO, Jul. 31–Aug. 4, 2006, pp. 3160–3163.
[20] R. J. Bullock, R. Voles, A. Currie, H. D. Griffiths, and P. V. Brennan, "Estimation and correction of roll errors in dual antenna interferometric SAR," in *Proc. IEE Radar*, Edinburgh, U.K., Oct. 14–16, 1997, pp. 253–257.
[21] A. Reigber, "Correction of residual motion errors in airborne SAR interferometry," *Electron. Lett.*, vol. 37, no. 17, pp. 1083–1084, Aug. 2001.
[22] P. Prats and J. J. Mallorqui, "Estimation of azimuth phase undulations with multisquint processing in airborne interferometric SAR images," *IEEE Trans. Geosci. Remote Sens.*, vol. 41, no. 6, pp. 1530–1533, Jun. 2003.
[23] A. Reigber, P. Prats, and J. J. Mallorqui, "Refined estimation of time-varying baseline errors in airborne SAR interferometry," *IEEE Geosci. Remote Sens. Lett.*, vol. 3, no. 1, pp. 145–149, Jan. 2006.
[24] H. Cantalloube and P. Dubois-Fernandez, "Airborne X-band SAR imaging with 10 cm resolution: Technical challenge and preliminary results," *Proc. Inst. Electr. Eng.—Radar Sonar Navig.*, vol. 153, no. 2, pp. 163–176, Apr. 2006.
[25] K. A. C. de Macedo, R. Scheiber, and A. Moreira, "An autofocus approach for residual motion errors with application to airborne repeat-pass SAR interferometry," in *Proc. IGARSS*, Barcelona, Spain, Jul. 23–27, 2007, pp. 4886–4889.
[26] A. L. Gray and P. J. Farris-Manning, "Repeat-pass interferometry with airborne synthetic aperture radar," *IEEE Trans. Geosci. Remote Sens.*, vol. 31, no. 1, pp. 180–191, Jan. 1993.
[27] A. Reigber and R. Scheiber, "Airborne differential SAR interferometry: First results at L-band," *IEEE Trans. Geosci. Remote Sens.*, vol. 41, no. 6, pp. 1516–1520, Jun. 2003.
[28] H. Zebker, P. A. Rosen, R. M. Goldstein, A. Gabriel, and C. Werner, "On the derivation of coseismic displacement fields using differential radar interferometry: The Landers earthquake," *J. Geophys. Res.*, vol. 99, no. B10, pp. 19 617–19 634, 1994.
[29] K. A. C. de Macedo and R. Scheiber, "Controlled experiment for analysis of airborne D-InSAR feasibility," in *Proc. EUSAR*. Ulm, Germany, May 25–29, 2004, pp. 761–764.
[30] J. Groot, "River dike deformation measurement with airborne SAR," *IEEE Geosci. Remote Sens. Lett.*, vol. 1, no. 2, pp. 94–97, Apr. 2004.
[31] G. Fornaro, R. Lanari, E. Sansosti, G. Francheschetti, S. Perna, A. Gois, and J. Moreira, "Airborne differential interferometry: X-band experiments," in *Proc. IGARSS*, Anchorage, AK, Sep. 20–24, 2004, vol. 5, pp. 3329–3332.
[32] K. A. C. de Macedo, C. Andres, and R. Scheiber, "On the requirements of SAR processing for airborne differential interferometry," in *Proc. IGARSS*, Seoul, Korea, Jul. 25–29, 2005, pp. 2693–2696.
[33] S. Perna, C. Wimmer, J. Moreira, and G. Fornaro, "X-band airborne differential interferometry: Results of the OrbiSAR campaign over the Perugia area," *IEEE Trans. Geosci. Remote Sens.*, vol. 46, no. 2, pp. 489–503, Feb. 2008.
[34] A. Moreira, J. Mittermayer, and R. Scheiber, "Extended chirp scaling algorithm for air- and spaceborne SAR data processing in stripmap and ScanSAR imaging modes," *IEEE Trans. Geosci. Remote Sens.*, vol. 34, no. 5, pp. 1123–1136, Sep. 1996.
[35] R. Scheiber and A. Moreira, "Coregistration of interferometric SAR images using spectral diversity," *IEEE Trans. Geosci. Remote Sens.*, vol. 38, no. 5, pp. 2179–2191, Jul. 2000.
[36] J. C. Curlander and R. N. McDonough, *Synthetic Aperture Radar: Systems and Signal Processing*. New York: Wiley, 1991.
[37] G. Franceschetti and R. Lanari, *Synthetic Aperture Radar Processing*. Boca Raton, FL: CRC, 1999.
[38] I. G. Cumming and F. H. Wong, *Digital Processing of Synthetic Aperture Radar Data. Algorithms and Implementation*. Boston, MA: Artech House, 2005.
[39] M. Y. Jin and C. Wu, "A SAR correlation algorithm which accommodates large-range migration," *IEEE Trans. Geosci. Remote Sens.*, vol. 22, no. 6, pp. 592–597, Nov. 1984.
[40] C. Cafforio, C. Prati, and F. Rocca, "SAR data focusing using seismic migration techniques," *IEEE Trans. Aerosp. Electron. Syst.*, vol. 27, no. 2, pp. 194–207, Mar. 1991.
[41] R. K. Raney, H. Runge, R. Bamler, I. Cumming, and F. H. Wong, "Precision SAR processing using chirp scaling," *IEEE Trans. Geosci. Remote Sens.*, vol. 32, no. 4, pp. 786–799, Jul. 1994.
[42] D. Blacknell, A. Freeman, S. Quegan, I. A. Ward, I. P. Finley, C. J. Oliver, R. G. White, and J. W. Wood, "Geometric accuracy in airborne SAR images," *IEEE Trans. Aerosp. Electron. Syst.*, vol. 25, no. 2, pp. 241–258, Mar. 1989.
[43] S. Buckreuss, "Motion errors in an airborne synthetic aperture radar system," *Eur. Trans. Telecommun. Relat. Technol.*, vol. 2, no. 6, pp. 55–64, Nov. 1991.
[44] G. Fornaro, "Trajectory deviations in airborne SAR: Analysis and compensation," *IEEE Trans. Aerosp. Electron. Syst.*, vol. 35, no. 3, pp. 997–1009, Jul. 1999.
[45] H. Qi and J. B. Moore, "Direct Kalman filtering approach for GPS/INS integration," *IEEE Trans. Aerosp. Electron. Syst.*, vol. 38, no. 2, pp. 687–693, Apr. 2002.
[46] P. Prats, K. A. C. de Macedo, A. Reigber, R. Scheiber, and J. J. Mallorqui, "Comparison of topography- and aperture-dependent motion compensation algorithms for airborne SAR," *IEEE Geosci. Remote Sens. Lett.*, vol. 4, no. 3, pp. 349–353, Jul. 2007.
[47] D. R. Stevens, I. G. Cumming, and A. L. Gray, "Options for airborne interferometric SAR motion compensation," *IEEE Trans. Geosci. Remote Sens.*, vol. 33, no. 2, pp. 409–420, Mar. 1995.
[48] P. Prats, A. Reigber, J. J. Mallorqui, P. Blanco, and A. Moreira, "Estimation of the deformation temporal evolution using airborne differential SAR interferometry," in *Proc. IGARSS*, Denver, CO, Jul. 31–Aug. 4, 2006, pp. 1894–1897.
[49] R. Bamler and M. Eineder, "Accuracy of differential shift estimation by correlation and split-bandwidth interferometry for wideband and Delta-k SAR systems," *IEEE Geosci. Remote Sens. Lett.*, vol. 2, no. 2, pp. 151–155, Apr. 2005.
[50] A. Reigber, "Airborne polarimetric SAR tomography," Ph.D. dissertation, Inst. Navigation der Univ. Stuttgart, Stuttgart, Germany, Oct. 2001.
[51] A. Reigber, "Range dependent spectral filtering to minimize the baseline decorrelation in airborne SAR interferometry," in *Proc. IGARSS*, Hamburg, Germany, Jun. 28–Jul. 2, 1999, vol. 3, pp. 1721–1723.
[52] M. Costantini and P. A. Rosen, "A generalized phase unwrapping approach for sparse data," in *Proc. IGARSS*, Hamburg, Germany, Jun. 28–Jul. 2, 1999, vol. 4, pp. 267–269.
[53] A. Reigber and J. Moreira, "Phase unwrapping by fusion of local and global methods," in *Proc. IGARSS*, Singapore, Aug. 3–8, 1997, vol. 2, pp. 869–871.
[54] A. Reigber and A. Moreira, "First demonstration of airborne SAR tomography using multibaseline L-band data," *IEEE Trans. Geosci. Remote Sens.*, vol. 38, no. 5, pp. 2142–2152, Sep. 2000.
[55] M. Nolan and D. R. Fatland, "Penetration depth as a DInSAR observable and proxy for soil moisture," *IEEE Trans. Geosci. Remote Sens.*, vol. 41, no. 3, pp. 532–537, Mar. 2003.

Pau Prats (S'03–M'06) was born in Madrid, Spain, in 1977. He received the Ingeniero degree in telecommunication engineering and the Ph.D. degree from the Universitat Politècnica de Catalunya (UPC), Barcelona, Spain, in 2001 and 2006, respectively.

In 2001, he was with the Institute of Geomatics, Barcelona, Spain, as a Research Assistant, designing a subaperture SAR processor. In 2002, he joined the Department of Signal Theory and Communications, UPC, where he worked in the field of airborne repeat-pass interferometry and airborne differential SAR interferometry. From December 2002 to August 2006, he was an Assistant Professor in the Department of Telecommunications and Systems Engineering, Universitat Autónoma de Barcelona (UAB), Barcelona. Since August 2006, he has been with the SAR Processing Group, Microwave and Radar Institute, German Aerospace Center (DLR), Oberpfaffenhofen, as a Research Scientist, working in the field of SAR processing and interferometry. His research interests include SAR processing, airborne motion compensation, single/repeat-pass interferometry, and differential interferometry with airborne systems.

Dr. Prats received the First Prize at the Student Paper Competition, International Geoscience and Remote Sensing Symposium 2005, Seoul, Korea.

Andreas Reigber (M'02) was born in Munich, Germany, in 1970. He received the Diploma degree in physics from the University of Constance, Constance, Germany, in 1997 and the Ph.D. degree from the University of Stuttgart, Stuttgart, Germany, in 2001.

From 1996 to 2000, he was with the Microwave and Radar Institute, German Aerospace Center (DLR), Oberpfaffenhofen, where he worked in the field of polarimetric SAR tomography. In 2001, he was with the Antenna, Radar, and Telecom Laboratories, University of Rennes 1, Rennes, France, for a postdoctoral position on radar polarimetry and polarimetric interferometry. Since 2002, he has been a Research Associate with the Computer Vision and Remote Sensing Laboratories, Berlin University of Technology, Berlin, Germany. His current main research interests include the various aspects of multimodal SAR, like SAR interferometry, SAR polarimetry, SAR tomography, and time–frequency analyses but also hyperspectral remote sensing and the application of computer vision and machine learning approaches in remote sensing.

Dr. Reigber was the recipient of the European SAR Conferences 2000 Student Prize Paper Award for an article on SAR remote sensing of forests, the IEEE GRSS Transactions Prize Paper Award in 2001 for a work on polarimetric SAR tomography, as well as the IEEE GRSS Letters Prize Paper Award in 2006 for a work on multipass SAR processing. He also coauthored three papers which have been successful at the student paper competitions of IGARSS'05 (first prize), EUSAR'06 (third prize), and IGARSS'07 (second prize).

Jordi J. Mallorquí (S'93–M'96) was born in Tarragona, Spain, in 1966. He received the Ingeniero degree in telecommunications engineering and the Ph.D. degree in telecommunications engineering for his research on microwave tomography for biomedical applications from the Universitat Politècnica de Catalunya (UPC), Barcelona, Spain, in 1990 and 1995, respectively.

In 1993, he was an Assistant Professor and, since 1997, he has been an Associate Professor with the Department of Signal Theory and Communications, UPC. His teaching activity involves microwaves, radio-navigation systems, and remote sensing. In 1999, he spent a sabbatical year with the Jet Propulsion Laboratory, Pasadena, CA, where he worked on interferometric airborne SAR calibration algorithms. He is currently working on the application of SAR interferometry to terrain deformation monitoring with orbital, airborne, and ground data, vessel detection and classification from SAR images, and 3-D electromagnetic simulation of SAR systems. He is also collaborating in the design and construction of a ground-based SAR interferometer for landslide control. Finally, he is currently developing the hardware and software of a bistatic oportunistic SAR for interferometric applications using ERS, ENVISAT, and TerraSAR-X as sensors of opportunity. He has published more than 80 papers on microwave tomography, electromagnetic numerical simulation, and SAR processing, interferometry, and differential interferometry in referred journals and international symposia.

Rolf Scheiber received the Diploma degree in electrical engineering from the Technical University of Munich, Munich, Germany, in 1994 and the Ph.D. degree in electrical engineering from the University of Karlsruhe, Karlsruhe, Germany, in 2003, with a thesis on airborne SAR interferometry.

Since 1994, he has been with the Microwaves and Radar Institute, German Aerospace Center (DLR), Oberpfaffenhofen, where he developed the operational high-precision interferometric SAR processor for its Experimental SAR (E-SAR) airborne sensor. Since 2001, he has been heading the SAR Signal Processing Group, SAR Technology Department, where he is presently responsible for the E-SAR campaign data processing, as well as the development of the processing software for the new airborne sensor F-SAR. His current research interests include algorithm development for high-resolution air- and spaceborne SAR focusing, SAR interferometry, differential SAR interferometry, SAR tomography, as well as radio-sounding algorithms and applications.

Dr. Scheiber received the IEEE TRANSACTIONS ON GEOSCIENCE AND REMOTE SENSING Transactions Prize Paper Award in 1997 as a coauthor of the contribution, "Extended Chirp Scaling Algorithm for Air- and Spaceborne SAR Data Processing in Stripmap and ScanSAR Imaging Modes."

Alberto Moreira (M'92–SM'96–F'04) was born in São José dos Campos, Brazil, in 1962. He received the B.S. and M.S. degrees in electrical engineering from the Aeronautical Technological Institute, São José dos Campos, in 1984 and 1986, respectively, and the Dr.Eng. degree (with honors) from the Technical University of Munich, Munich, Germany, in 1993.

From 1996 to 2001, he was a Chief Scientist and Engineer with the SAR Technology Department, Microwaves and Radar Institute, German Aerospace Center (DLR), Oberpfaffenhofen, where since 2001, he has been the Director with the Microwaves and Radar Institute. The institute contributes to several scientific programs and space projects for actual and future air- and spaceborne SAR missions. Recently, the mission proposal TanDEM-X led by his institute has been approved for the realization phase. He is the Initiator and Principal Investigator for this mission. In 2003, he was a Full Professor in the field of microwave remote sensing with the University of Karlsruhe, Karlsruhe, Germany. He pioneered research on high-resolution radar signal processing and innovative SAR system concepts and associated techniques like radar tomography, digital beamforming, and advanced imaging modes. His professional interests and research areas encompass radar end-to-end system design and analysis, innovative microwave techniques and system concepts, signal processing and remote sensing applications.

Prof. Moreira is currently serving as a member of the IEEE GRSS Administrative Committee (1999–2001, 2004–2009), has been the Chair of the German Chapter, GRSS, since 2003, and is currently actively serving as an Associate Editor for the IEEE GEOSCIENCE AND REMOTE SENSING LETTERS. Since 2003, he has also been serving as a member of the Board of Directors of the Information Technology Society of VDE (German Association for Electrical, Electronic, and Information Technologies). In 1995, he was the recipient of the DLR Science Award. He and his colleagues were the recipients of the GRSS Transactions Prize Paper Awards in 1997 and 2001. He was also the recipient of the IEEE Nathanson Award in 1999 and the IEEE Kiyo Tomiyasu Award in 2007. He has been contributing to the successful series of the European SAR conferences since 1996 as a member of the Technical Program Committee, as Technical Chairman in 2000, as an Awards Chairman from 2002 to 2004, and as a General Chairman in 2006.